Dual-rotation C-arm cone-beam computed tomography to increase low-contrast detection

Aymeric Reshef[a)]
LTCI, Télécom ParisTech, Université Paris-Saclay, 75013, Paris, France
GE Healthcare, Buc, France

Cyril Riddell and Yves Trousset
GE Healthcare, Buc, France

Saïd Ladjal and Isabelle Bloch
LTCI, Télécom ParisTech, Université Paris-Saclay, 75013, Paris, France

(Received 3 October 2016; revised 17 February 2017; accepted for publication 23 March 2017; published 13 September 2017)

Purpose: This paper investigates the capabilities of a dual-rotation C-arm cone-beam computed tomography (CBCT) framework to improve non-contrast-enhanced low-contrast detection for full volume or volume-of-interest (VOI) brain imaging.
Method: The idea is to associate two C-arm short-scan rotational acquisitions (spins): one over the full detector field of view (FOV) at low dose, and one collimated to deliver a higher dose to the central densest parts of the head. The angular sampling performed by each spin is allowed to vary in terms of number of views and angular positions. Collimated data is truncated and does not contain measurement of the incoming X-ray intensities in air (air calibration). When targeting full volume reconstruction, the method is intended to act as a virtual bow-tie. When targeting VOI imaging, the method is intended to provide the minimum full detector FOV data that sufficiently corrects for truncation artifacts. A single dedicated iterative algorithm is described that handles all proposed sampling configurations despite truncation and absence of air calibration.
Results: Full volume reconstruction of dual-rotation simulations and phantom acquisitions are shown to have increased low-contrast detection for less dose, with respect to a single-rotation acquisition. High CNR values were obtained on 1% inserts of the Catphan® 515 module in 0.94 mm thick slices. Image quality for VOI imaging was preserved from truncation artifacts even with less than 10 non-truncated views, without using the sparsity a priori common to such context.
Conclusion: A flexible dual-rotation acquisition and reconstruction framework is proposed that has the potential to improve low-contrast detection in clinical C-arm brain soft-tissue imaging. © *2017 American Association of Physicists in Medicine* [https://doi.org/10.1002/mp.12247]

Key words: bow-tie filter, brain imaging, cone-beam computed tomography, iterative reconstruction, low-contrast detection, volume-of-interest

1. INTRODUCTION

C-arm cone-beam computed tomography (CBCT) plays a growing role in interventional neuroradiology, thanks to the high spatial resolution it provides for vascular imaging. In particular, dual-rotation, one with intra-arterial injection of iodinated contrast agent and one without, allows for the 3D reconstruction of very fine vessels using subtraction.[1] However, non-contrast-enhanced imaging of soft tissues in the brain remains particularly challenging. C-arm CBCT has inferior contrast detection because images are contaminated by scatter and lack uniformity, and because lower contrasts require delivering more dose. CT scanners achieve low-contrast detection because they reject most scattered radiations, and allow more dose to be locally delivered to the patient head by modulating the incoming x-ray beam intensities with a bow-tie filter, which also flattens the noise profile over the detector and the reconstructed field-of-view (FOV).[2–5] Uniformity would also be altered by truncation. CT scanners' long detectors avoid this issue.

The mechanical flexibility provided by C-arm systems does not allow for efficient scatter rejection and the small number of C-arm CBCT acquisitions of brain soft tissues that need to be performed per day does not warrant the expensive integration of a bow-tie filter dedicated to this specific imaging task. Without a bow-tie filter, higher intensities must be recorded on the detector together with a wider dynamic range. This is a challenge for flat-panel detectors, that must be addressed by improved detector readout techniques.[6,7] Higher scatter fraction must be corrected separately prior to reconstructing the image.[8,9] There is thus an interest in designing an acquisition with a nonuniform exposure delivering better measurements with less dose to the patient.

Interestingly, C-arm CBCT is often used for volume-of-interest (VOI) imaging, with limited contrast detection due to truncation artifacts. Building upon the concept of the bow-tie filter, several beam modulators have been proposed to concentrate the exposure over the VOI while avoiding truncation artifacts.[10–19] Beam modulators for VOI imaging are again invasive and costly to integrate, lacking flexibility since they

only define a fixed aperture. Another common approach has thus been to use two sets of projections: one bearing most of the exposure and sampling the VOI, and the other acquired at a reduced dose from which it is possible to (a) reconstruct a "good-enough" image of the entire object that (b) allows the computation of the missing data to complete the truncated projections.[20–29] All approaches concur in providing the missing data at a low dose because truncation artifacts are due to truncated low frequencies and low frequencies can be captured at high noise and reconstructed with strong smoothing. They also concur in reducing the dose per view rather than the number of views if no a priori information is available. Although beam modulators provide a fixed dose ratio, separate acquisitions are more flexible, but since the incoming x-ray beam cannot be measured in the truncated aperture, means to estimate its intensity must be provided to avoid biases between the low-dose, low-frequency signal and the truncated one (e.g., Ref. [24]).

In the context of C-arm CBCT, we propose to study the capabilities of a dual-rotation acquisition to improve low-contrast detection when not only imaging the full brain without administration of contrast agent but also when performing VOI imaging. The proposed dual rotation consists of two short-scan circular rotations ("spins"), one over the full detector FOV and the second with a detector FOV that is reduced by collimation. This acquisition can sample the brain with three degrees of freedom: (a) the aperture of the truncated spin, (b) the dose ratio between both spins, and (c) the number of views per spin. They allow us to either emulate a bow-tie filter to increase low-contrast detection or to perform VOI imaging with little extra-exposure and limited truncation artifacts. For both cases, we design a single iterative reconstruction algorithm that does not require knowledge of the incoming x-ray beam intensity of the truncated data nor that the views be acquired at the exact same positions.

Section 2.A describes our acquisition framework with respect to truncation, dose, and angular sampling per rotation. Our iterative reconstruction is explicated in Section 2.B. Experiments on simulated data and acquisitions of a quality assurance phantom and of anthropomorphic head phantoms are presented in Section 3. Reconstruction results are presented in Section 4. The clinical relevance of the method is discussed in Section 5.

2. METHODS

2.A. Dual-rotation acquisition

2.A.1. Assumptions

Ideal system measurements are intensity projections I related to density projections p via Beer's law $I = I_0 e^{-p}$ where I_0 is the intensity of the x-ray beam measured in air. We assume that prior calibration steps transformed the open-field intensities into a constant I_0 value on the detector. Intensity projections are related to object density f through a linear projection operator R such that $Rf + \log(I) = \log(I_0)$. Of course, real data are also corrupted by noise and scattered radiations.

We consider two sets of intensity projections (Fig. 1): one set of full-FOV projections (indexed by F), and one set of truncated projections (indexed by T). In order to mimic a bow-tie filter for dose optimization, the full-FOV spin is acquired at low dose—this prevents unnecessary patient dose—while the truncated spin is acquired at a higher dose to achieve an exposure target at the center of the imaged object that is thicker. We intend the dual-rotation acquisition to be as little restrictive as possible:

- we do not assume to know the exposure ratio between the full-FOV spin and the truncated spin, even though truncated data do not contain a reference air measurement of the incoming x-ray beam;
- we do not assume the geometry to be the same for each acquisition; in particular, the angular sampling may vary both in terms of angular positions and number of projection views.

2.A.2. Parameters

The flexibility of the dual-rotation acquisition comes from three degrees of freedom.

(i) First, although one acquisition is always assumed to be full-FOV, the opening of the truncated FOV is a free parameter; we denote by t, $0 < t \leq 1$, the level by which truncation reduces the exposed detector area as compared to the un-collimated case.
(ii) Secondly, we do not impose any constraint on the intensity ratio that is used between the two acquisitions: if I_0^{F} denotes the air intensity corresponding to the exposure at the center of the object achieved with the full-FOV spin and I_0^{T} is the intensity of the truncated spin, we write $x = I_0^{\mathrm{T}}/I_0^{\mathrm{F}}$, so that the actual exposure at the center of the object is equal to $(1+x)I_0^{\mathrm{F}}$ in the dual-rotation acquisition. Putting aside a dual-energy approach, x is simply the mAs ratio.

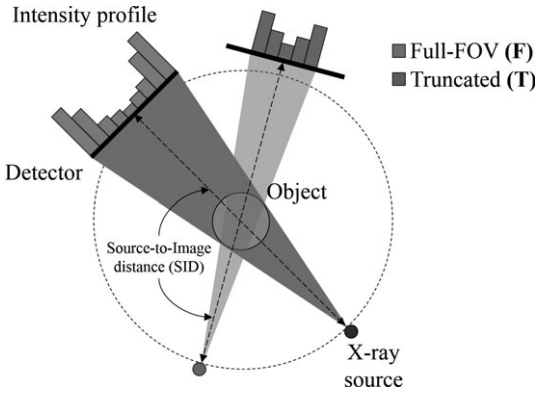

FIG. 1. Dual-rotation acquisition: a set of N_{T} truncated projections is acquired at the dose required by the central thickest areas and a set of N_{F} full-FOV projections is acquired at a lower dose, sufficient for the less dense, external areas.

(iii) Thirdly, we allow the number of views to change from one spin to the other. In the following, we always assume that projection views are uniformly sampled over the short-scan, and we further write $s = N_T/N_F$.

2.A.3. Virtual bow-tie

To emulate a bow-tie that increases low-contrast detection over the full volume, we choose $x \geq 1$. Truncation is controlled by t and depends on the targeted dose optimization. In configuration $s = 1$, both spins finely sample the acquisition orbit. We also explore the case $s < 1$.

We define the dose reduction factor d as how much dose to the object is saved with the dual-rotation acquisition as compared to an equivalent single-rotation, full-FOV acquisition achieving the same exposure level at the center of the object. This factor is thus equal to:

$$d = \frac{N_F I_0^F + N_T I_0^T}{N_F I_0^F + t \cdot N_T I_0^T} = \frac{1 + xs}{1 + txs}. \quad (1)$$

2.A.4. VOI imaging

In the case of VOI imaging, the truncation parameter t defines the VOI. The full-FOV projections are now used as additional information to compensate for the missing data, and we still choose an intensity ratio $x \geq 1$, as the full-FOV spin still samples less dense areas. However, rather than trying to maximize x as commonly reported in the literature, we look at increasing s in order to both decrease dose and lower the acquisition time.

2.B. Reconstruction

Given (t,x,s), we define the contribution of the full-FOV acquisition to the overall dose as

$$\alpha_F = \frac{N_F I_0^F}{N_F I_0^F + N_T I_0^T} = \frac{1}{1 + xs}. \quad (2)$$

Reciprocally, we define the contribution of the truncated acquisition as $\alpha_T = 1 - \alpha_F$.

2.B.1. Analytical reconstruction

If intensity spins I_T and I_F were acquired at the very same angular positions, the data could be blended according to

$$p = \begin{cases} \alpha_F \cdot p_F + \alpha_T \cdot p_T & \text{in the collimated area,} \\ p_F & \text{elsewhere.} \end{cases} \quad (3)$$

Equation (3) is sensitive to offset errors in p_F or p_T. In C-arm CBCT, projections are acquired with short-scan circular rotations ("spins"). They are reconstructed with the Feldkamp–Davis–Kress (FDK) algorithm[30] using Parker's weights to account for data redundancy.[31] We denote $f_{FDK} = R_W^{TDp}$ this analytical reconstruction, with p_W the Parker-weighted version of density projections p, D the ramp filter, and R^T the transpose of R, that is the backprojection operator.

If acquisition geometries are different, there is no standard solution and for each situation clever resampling or extrapolation of the truncated data must be derived. We instead propose a unique iterative algorithm to handle all dose and sampling configurations.

2.B.2. Energy minimization

We define two quadratic forms for $n \in \{F,T\}$

$$\mathcal{Q}_n(f) = \frac{1}{2}(R_n f + \log(I_n))^T D_n (R_n f + \log(I_n)), \quad (4)$$

where R_F (resp. R_T) is the projection operator for the untruncated (resp. truncated) geometry, and D_F (resp. D_T) is the ramp filtering operator for untruncated (resp. truncated) signals.

Since $\log(I_n)$ is known instead of the density projections p_n, we cannot reconstruct an image f such that $R_n f + \log(I_n) = \log(I_0^n)$ but only such that

$$D_n(R_n f + \log(I_n)) = D_n(\log(I_0^n)) = 0. \quad (5)$$

Consequently, D_n must remove any unknown offset $\log(I_0^n)$.

We minimize both data fidelity terms simultaneously through:

$$\underset{f}{\operatorname{argmin}} \left\{ \sum_{n \in \{F,T\}} \alpha_n \mathcal{Q}_n(f) + \chi(f) \right\}, \quad (6)$$

where $\chi(f)$ is a convex regularizing term.

Quadratic forms like $\mathcal{Q}_n(f)$ have already been used[32] with sparsity-enforcing regularizers to correct for angular subsampling and cone-beam artifacts. Dual-rotation, however, is aimed at avoiding the need for a strong a priori like sparsity. Therefore, we used a small quadratic regularization $\chi(f) = \lambda \| \nabla f \|^2$ that is known to induce a Gaussian diffusion with full width at half maximum (FWHM) equal to $3.33\sqrt{\lambda}$.[33] Following Ref. [32], we solved Eq. (6) using a forward-backward splitting scheme.

2.B.3. Ramp-filtering operators

Row-wise ramp filtering of the projection data is usually performed in the Fourier space. It has been reported[34] that for acurate FDK reconstruction, the discrete ramp filter should be computed as the Fourier transform of the finite spatial ramp kernel. Yet this results in a nonzero DC value, which does not satisfy $D_n(\log(I_0^n)) = 0$.

Instead we take advantage of the decomposition of the ramp filter into a derivative operator ∂_u and a Fourier-based Hilbert transform H. Applying ∂_u guarantees that $D_n(\log(I_0^n)) = 0$.

We write

$$D_F = H \partial_u. \quad (7)$$

In the case of D_T, ∂_u is local and applied within the truncated FOV. However, the Fourier-based Hilbert transform needs data extrapolation. The residual $R_T f + \log(I_T)$ is expected to converge to a constant that cannot be zero-padded. Instead, extrapolation of $\partial_u(R_T f + \log(I_T))$ with zeroes prior to computing the Fourier-based Hilbert transform makes perfect sense. However, nonidealities in the data may still introduce some undesirable discontinuities near the truncation boundaries. To ensure a smooth transition, a Hanning window is applied to the residual *after* it is differentiated. The minimization problem (6) thus actually uses two different operators D_F and D_T, where D_F is defined in Eq. (7) and

$$D_T = HW\partial_u, \tag{8}$$

with W being the Hanning apodization operator.

3. EXPERIMENTS

3.A. Simulations

For the bow-tie emulation, $s = 1$ and the dose reduction factor has two degrees of freedom x and t; we arbitrarily fixed $x = 4$, and determined through simulations which truncation width t would provide the best approximation to a true bow-tie to flatten the noise distribution in the reconstructed images. An analytical density sinogram p was computed and consisted of 600 profiles in parallel-beam geometry of a centered disk with diameter 15 cm and density $\mu = 0.376\ \text{cm}^{-1}$. I_0^F was fixed to 10^5 to generate two intensity sinograms I_F and I_T corrupted by Gaussian approximations of Poisson noise, further transformed into noisy densities $p_F = \log(I_0^F) - \log(I_F)$ and $p_T = \log(I_0^T) - \log(I_T)$. Sinogram p_T was then digitally truncated by keeping a fraction t of the initial FOV (Fig. 2(a)). Projections p_F and p_T were then blended according to Eq (3). The blended sinogram is equivalent to a single acquisition at high dose, using an ideal beam filter that absorbs five times more energy at its peripheries. We generated 100 pairs of noisy sinograms at low and high dose, yielding 100 reconstructed images per value of t.

We also generated 100 sinograms using $I_0 = I_0^T + I_0^F$ and a simulated bow-tie filter perfectly compensating the shape of the disk, by computing a flat, noisy sinogram further divided by the gain map of the bow-tie filter. All reconstructions were performed using data blending and analytical (FBP) reconstruction. Maps of the pixel-wise standard deviation were computed using all replicate reconstructions. Since the simulated phantom is rotationally invariant, we computed a radial averaging to obtain radial profiles characteristic of the noise distribution.

3.B. Acquisitions

3.B.1. Phantoms

We tested the dual-rotation framework on the Catphan®[35] and on two anthropomorphic head phantoms. For the Catphan®, we used the 515 low-contrast detection module, the 486 uniformity module, and the 528 high-resolution module. The 515 module contains low-contrast inserts with nominal relative contrasts of 1%, 0.5%, and 0.3%. Their diameters vary from 2 mm to 15 mm. The diameters of the central (subslice) inserts vary from 3 mm to 9 mm. Their nominal contrast is 1%, with lengths of 3 mm, 5 mm, and 7 mm in the axial direction. One head phantom contains a few brain soft-tissue-like structures, the other is a skull filled with a uniform tissue-equivalent material.

3.B.2. Parameters

Acquisitions were performed on an IGS-740 C-arm system (GE Healthcare, Chicago, IL, USA). The IGS-740 flat-panel detector has a size of 40 cm × 40 cm, resulting in 500 × 500 projection images with pixels of size 0.8 mm × 0.8 mm.

The source-to-object distance (SOD) is 820 mm. The source-to-image-distance (SID) was set at 1295 mm, yielding a magnification factor of 1.58. The full-FOV width was always 40 cm. The FOV height was first set at 5.8 cm to minimize scattered radiation, leading to an anatomical coverage of 3.7 cm. Each spin was acquired as a single acquisition, then dual-rotation spin pairs were formed associating one full-FOV spin with a truncated spin of same FOV height and

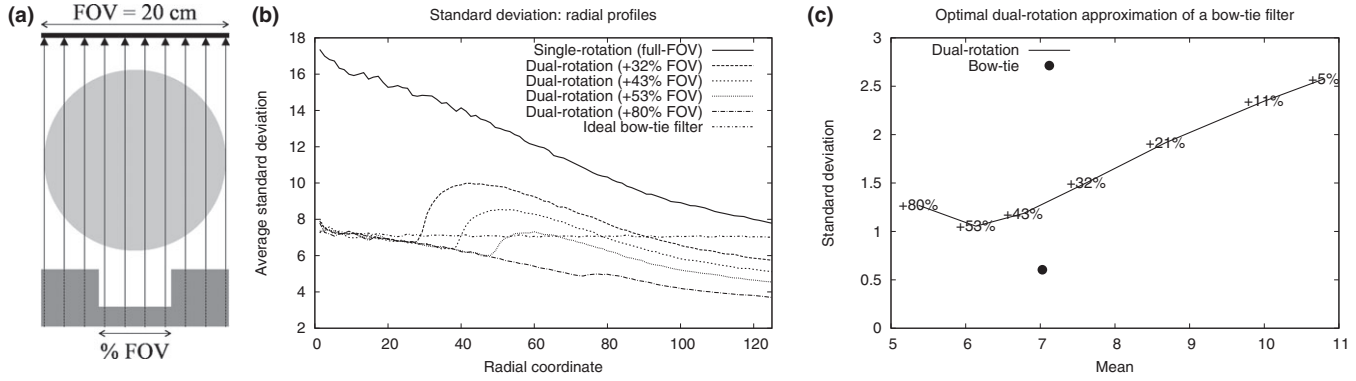

FIG. 2. Simulations of equivalent noise distribution in dual-rotation. (a) Simulation setting in parallel-beam geometry (see Section 3.A). (b) Radial profiles of the standard deviations of reconstructed images using FBP, with a single acquisition only and with different truncated FOV. (c) Noise uniformity, computed as the standard deviation of the noise radial profiles from (b) as a function of their mean values.

same truncation $t = 0.6$. For each pair, both spins uniformly sampled the 194° short-scan circular orbit, and at least one spin had 607 views (16°/s rotation at 50 views per second).

In order to test a larger anatomical coverage, one pair of spins was acquired with a FOV height of 15.6 cm, corresponding to a coverage of 9.9 cm. For this case, the truncated spin was acquired at a faster gantry rotation speed (28°/s at 50 views per second), yielding 347 projections. For VOI imaging, spins with less views were obtained by digital uniform down-sampling by varying s from 8 to 128, yielding sets of 4–75 full-FOV projections. On a separate experiment, truncation was applied digitally.

For x-ray exposure techniques the system automatic exposure control (AEC) would use 80 kVp for the head. For the Catphan®, we decided to use 120 kVp to generate intensities beyond the usual clinical practice in order to reach the higher dose levels needed for resolving lower contrast inserts. The current was set to 3.4 mAs for the high dose, truncated projections and 0.85 mAs for the low-dose full FOV spins (hence $x = 4$). The readout is achieved via a single-gain mode and was not changed between acquisitions. Thus, for the highest intensities (120 kVp×3.4 mAs), the detector readout would saturate for thicknesses lower than a few centimeters.

3.C. Reconstructions

Reconstructed images have isotropic voxels of size 0.94 mm. We used 50 iterations with a gradient step of 0.9. The quadratic regularization strength was always set to an FWHM of 1 voxel. Using these settings, the reconstruction of the Catphan® 528 module resolved the five line pairs per centimeter target (image not shown). For comparison purposes, single-rotation iterative reconstructions were obtained using $\alpha_F = 1$ for the full-FOV spin and $\alpha_T = 1$ for the truncated one.

3.D. Image quality measures

The Catphan® 515 module was used to evaluate the performance of the dual-rotation framework in terms of contrast detection.

The contrast was measured for the inserts listed in Table II. The background region was defined as a hollow cylinder around the target contrast insert with mean μ_{bkg}, and the foreground region was defined as a plain cylinder with a smaller radius, completely included in the contrast insert, and whose mean value is denoted by μ_{fg}. Each average was computed over at least 36 voxels.

Noise was estimated from two volumes f_1 and f_2 reconstructed from two replicated projection sets, each one being a statistical realization of the same acquisition protocol (either single-rotation or dual-rotation). By doing so, volume $\Delta = f_1 - f_2$ contained noise only. Since the Catphan® can be considered rotationally invariant, noise was estimated in K concentric hollow cylinders Ω_k containing all voxels of radius $r_{k-1} \leq r < r_k$.

The radial sampling $\{r_1,\cdots,r_K\}$ was nonuniform in order to keep the total number of voxels $|\Omega_k|$ approximately constant. With a cylinder height of eight slices, this number was equal to 805. We, thus, computed the radial standard deviation as

$$\sigma(\Omega_k) = \sqrt{\frac{1}{|\Omega_k|}\sum_{v\in\Omega_k}\frac{1}{2}\Delta^2(v)}. \quad (9)$$

The contrast-to-noise ratios (CNR) of insert i belonging to hollow cylinder Ω_j was then computed as

$$\mathrm{CNR}(i) = \frac{|\mu_{fg} - \mu_{bkg}|}{\sigma(\Omega_j)}.$$

4. RESULTS

4.A. Simulations

The simulated noise distributions are shown in Fig. 2(b). The single-rotation case corresponds to the FBP reconstruction from p_F only, which means that the entrance dose profile is uniform. The noise is much higher at the center of the disk than at its periphery. On the contrary, the noise distribution produced by the bow-tie filter shows a flat profile.

Dual-rotation shows an intermediate behavior. The tail of the noise standard deviation has globally the same shape as in the single-rotation case, and characterizes an unnecessary high dose in the peripheral areas. But at the center of the disk, the noise standard deviation matches the case of a bow-tie filter, as was targeted. A transition between the two FOV creates a bump that is stronger as t gets smaller. Figure 2(c) shows that when t gets higher, noise decreases significantly at the periphery of the disk and that when t is lower, the image is noisier. Using $t \approx 0.4-0.6$ provided the lowest variability of the radial profiles, while $t \approx 43\%$ matches the profile mean level of the bow-tie (black dot).

In these simulations, blended density sinograms were reconstructed with FBP, since air intensity measurements are perfectly known. We now show the results on real phantom data using our dedicated reconstruction method.

4.B. Virtual bow-tie

4.B.1. Catphan® phantom

The dose-area products (DAP) were the one reported by the system and corresponding to the system uniform exposure. They are summarized in Table I. Summing the DAPs of the truncated, high-dose acquisition (first row) and of the full-FOV, low-dose acquisition (second row) yields the DAP of the dual-rotation acquisition (third row). The equivalent single-rotation acquisition corresponds to the case of a unique full-FOV rotation achieving the same dose level at the center of the object. The equivalent DAP is obtained by summing five times the DAP of the full-FOV, low-dose acquisition (fourth row). The empirical dose reduction factor is calculated by dividing the DAP of the single-rotation

TABLE I. Dose-area products (dGy·cm^2) for the dual-rotation acquisition and for the equivalent single-rotation acquisition achieving the same dose at the center of the phantom.

Phantom	Catphan	Soft-tissue head
Truncated, 3.4 mAs	60.0	13.3
Full-FOV, 0.85 mAs	26.8	7.7
Dual-rotation	86.8	21.0
Equivalent single-rotation	134.1	38.5

acquisition by the DAP of the dual-rotation acquisition, yielding $d_{emp} = 1.54 \approx d$.

Figure 3(a) shows an axial slice of the 515 low-contrast detection module. The image is flat, but the noise level prevents a good visualization of the inserts. Fig. 3(b) is the dual-rotation reconstruction without smoothing the differentiated residual of the truncated data with a Hanning window. The image is already improved in terms of noise reduction and contrast detection; however, intense streaks are reconstructed as well. Fig. 3(c) shows the dual-rotation reconstruction using the additional smoothing with a Hanning window. The image shows a uniform background with lower noise. The improvement extends beyond the truncated FOV, as the backprojection operator redistributes density projections along the entire projection lines. Low-contrast inserts thus become visible and the truncated FOV introduces no artifact.

Noise radial standard deviations are shown in Fig. 4. The noise in the single-rotation reconstruction from the full-FOV spin is almost uniform, and tends to be lower at the periphery of the Catphan®. The dual-rotation reconstructed image shows a similar behavior, with much less noise. One can observe that the ratio between both curves varies from 1.9 to 2.6, with an average gain of 2.4. The CNR values for a set of inserts are given in Table II. If we set a detectability index as CNR≥1, all inserts of the Table II are detected with high confidence, except the less dense one of 0.3% at 15 mm that is borderline.

Figure 5 shows an axial slice cutting the 515 module at the same position as in Fig. 3 and a coronal slice cutting through the center of both the 515 and the 518 modules, which have different attenuations. The figure compares the iterative reconstruction from the full-FOV acquisition only and the dual-rotation reconstruction at a larger FOV height for the same truncation level $t = 0.6$. The reconstructed image from the low-dose, full-FOV spin is now both noisy and corrupted by scattered radiations, which results in a contrast loss. Associating this spin with the high-dose, truncated spin, which is less corrupted by scattered radiations, results in a visually more uniform and less noisy image, despite a residual cupping.

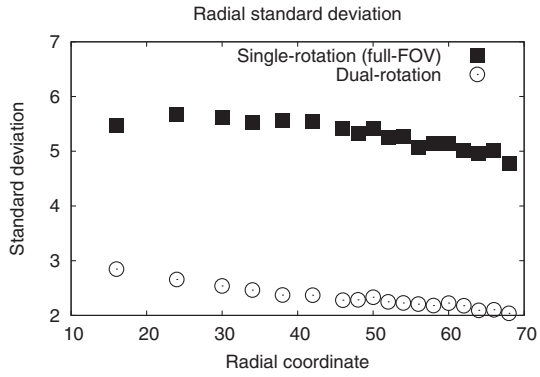

FIG. 4. Noise radial standard deviation for the single- and dual-rotation reconstructed images of the Catphan®.

TABLE II. CNR of single- and dual-rotation reconstructions of the Catphan® 515 (Figs. 3(a) and 3(c)).

Nominal contrast	Diameter	Single	Dual
1.0%	15 mm	1.5	2.8
0.5%	15 mm	1.0	2.0
0.3%	15 mm	0.5	1.0
1.0%	7 mm (length: 7 mm)	1.0	2.6
1.0%	7 mm (length: 5 mm)	0.8	1.8
1.0%	7 mm (length: 3 mm)	1.4	3.0

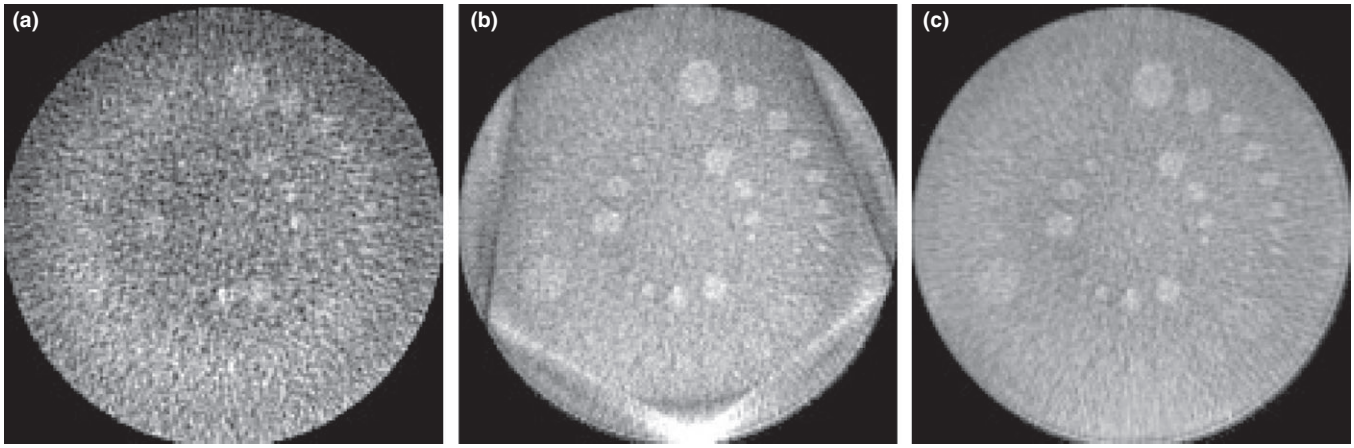

FIG. 3. (a) Single-rotation reconstruction from the full-FOV, low-dose spin. (b) Dual-rotation reconstruction without using the Hanning window in Eq. (8). (c) Dual-rotation reconstruction. Isotropic voxel size: 0.94 mm. Window width is 50 HU.

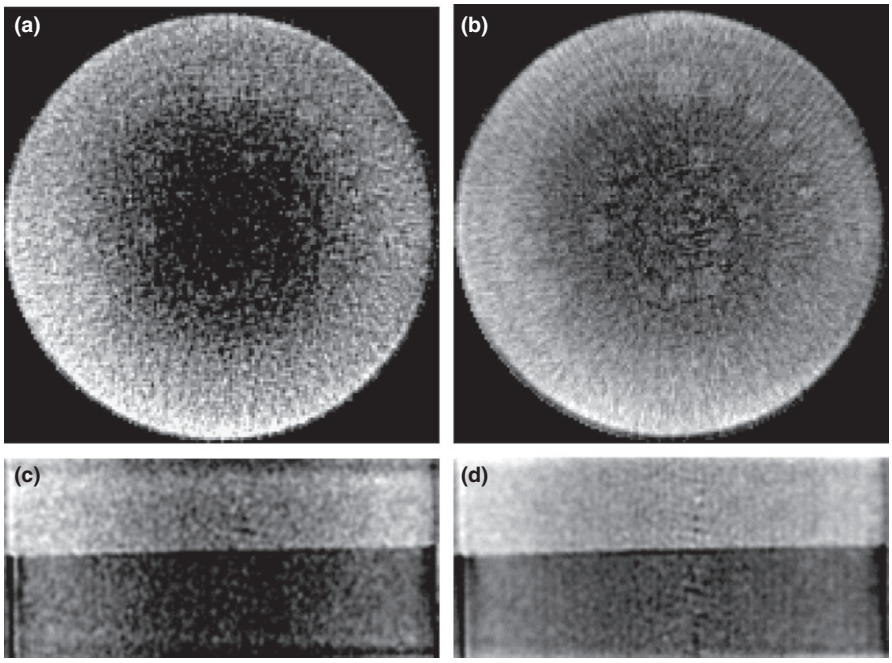

FIG. 5. Reconstructed images from acquisitions at a 3D FOV height of 9 cm. (a): Iterative reconstruction from the full-FOV acquisition only. (b): Dual-rotation reconstruction. (c) (resp. (d)): coronal slice of (a) (resp. (b)). Isotropic voxel size: 0.94 mm. Window width is 50 HU for (a),(b) and 75 HU for (c),(d).

4.B.2. Soft-tissue head phantom

Figure 6(a) shows the reconstruction from the low-dose, full-FOV spin only. Again, the image is flat but noisy. Figure 6(b) shows the dual-rotation reconstruction. We observe no visible artifact coming from the fact that a truncated spin is involved in the reconstruction. Thus, image quality fully benefits from the noise reduction.

For instance, the arrows in Fig. 6 point to a thin, low-contrasted structure that was lost in noise in Fig. 6(a) and was restored in Fig. 6(b).

4.C. VOI imaging

When no full-FOV view is available (Fig. 7(a)), the quadratic criterion does not bring in any a priori information and performs no better than what would be obtained with an analytical reconstruction with extrapolation.

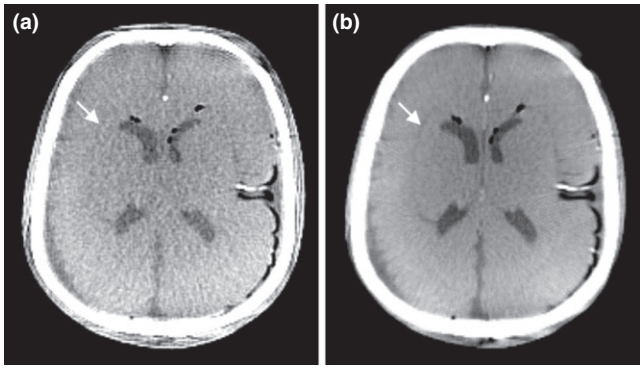

FIG. 6. Iterative reconstructions of the soft-tissue head phantom from (a) a single low-dose, full-FOV spin, (b) a dual-rotation acquisition. Isotropic voxel size: 0.94 mm. Window width is 150 HU.

The association with nine low-dose, full-FOV projections yields an image with severe distortions outside the VOI, but provides a much better uniformity inside, as shown in Fig. 7(b). At 19 projections (Fig. 7(c)), the cupping within the VOI is entirely removed and all inserts can be seen as well as in Fig. 7(d) where all full-FOV views have been used for the reconstruction. The plot of Fig. 8 shows the central profiles through the VOI, after subtracting each profile with its mean value to remove DC-shifts that also affect the reconstruction of truncated data. It confirms how a small number of full-FOV projections flattens the profiles.

Figure 9 shows the reconstructions of the uniform head phantom acquisition for $s = 16$ to 128, after it has been digitally truncated right through the skull bones, a case that no simple extrapolation can compensate. Again, when no full-FOV view is available, the quadratic criterion does not perform any better than an analytical reconstruction. The skull outside the VOI is not even visible in the windowing of Fig. 9(a), but appears heavily distorted with the first subset of four full-FOV views (Fig. 9(b)). As the number of full-FOV views is increased, the distortions disappear progressively outside the VOI and, most interestingly, much more quickly within the VOI (Figs. 9(b)–9(f)). The profiles taken through the line shown in Fig. 9(a) were similar and flat as soon as full-FOV views were introduced. However, they differed by DC shifts of 20% maximum for $s = 128$ (graph not shown). Once corrected for these offsets, absolute values of the errors with respect to the profile of the reference image (Fig. 9(f)) are shown as histograms in Fig. 10).

This measurement singles out the truncated case as much worse than when even four views only are introduced in the

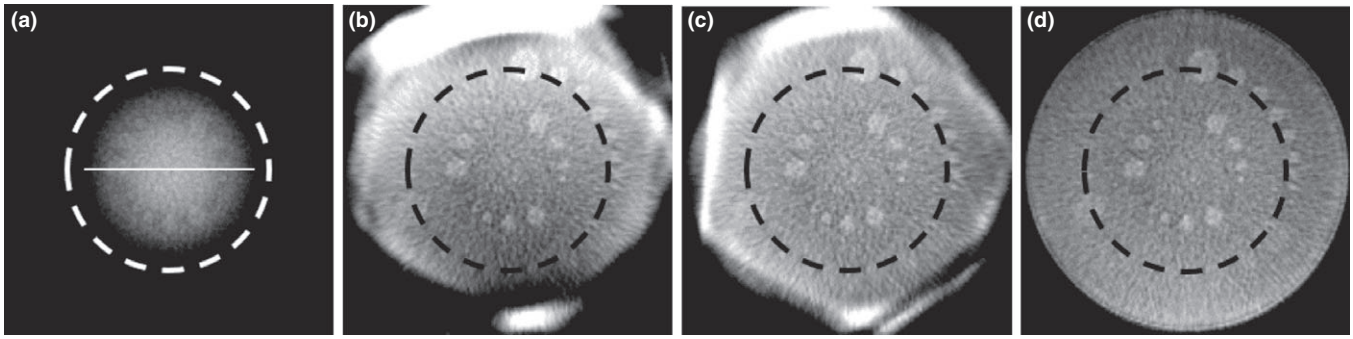

FIG. 7. Dual-rotation VOI imaging of the Catphan® 515 module. (a) Single-rotation iterative reconstruction. (b),(c) Dual-rotation reconstructions using (b) 9 projections, and (c) 18 projections. (d) Dual-rotation reconstruction using the fully sampled full-FOV spin. The truncated FOV is shown as a dashed circle.

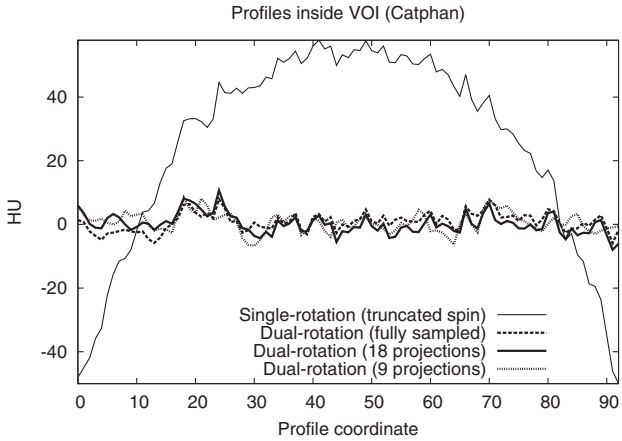

FIG. 8. Dual-rotation VOI imaging: deviations from the mean line profiles values. The line profile is the one drawn in Fig. 7(a).

reconstruction criterion. The bar chart, however, does not show a consistent error reduction with respect to the increasing number of views: the case $s = 128$ has less voxels with errors greater than 3% than cases $s = 64$ and $s = 32$. This is possible due to the fact that it only captures part of the error, as it does not take into account the DC shift. We find that the DC shift is consistently reduced by increasing the number of views. The fact that the entire skull had been truncated did not change the behavior of the dual-rotation framework with respect to the Catphan® case: what appears as distortions outside the VOI is a sufficiently good depiction of the missing low frequencies to correct for truncation artifacts within the VOI.

5. DISCUSSION

Dual-rotation CBCT routinely provides three-dimensional digital subtracted angiography.[1] Cardiac imaging is achieved via multiple sweeps of the C-arm gantry as well.[36] Here, we show that dual-rotation is also suitable for improved noncontrast-enhanced low-contrast detection in brain imaging.

An iterative reconstruction algorithm was designed to handle the three degrees of freedom of the dual-rotation: truncation level t, dose ratio between spins x, and ratio of views per spin s.

It simultaneously reconstructs two spins in a single volume, without merging measurements in the projection domain, in order not to require the knowledge of the incoming x-ray beam intensities in the truncated views, or that measurements be taken at the exact same position twice. This thus puts no specific constraints on the mechanical design, but puts more weight on the computation infrastructure. As we mentioned, if the mechanical design is made precise enough to sample the exact same positions twice, analytical reconstruction is sufficient for full volume imaging. Let us emphasize that the proposed iterative reconstruction has more flexibility than a standard formulation. The optimization criterion directly handles the logarithm of the intensities $\log(I_n)$, not the density projections. Filtering with zero-padding of the

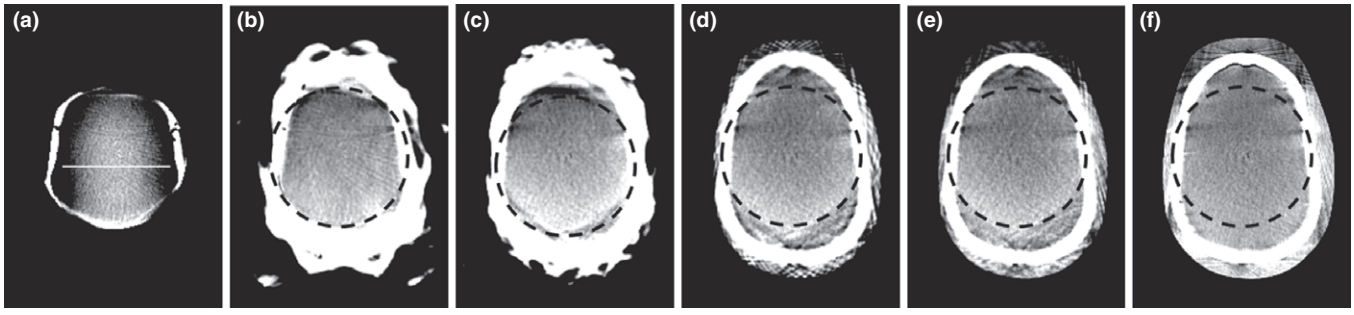

FIG. 9. Dual-rotation VOI imaging of a head phantom consisting of a skull with uniform soft tissues. (a): Iterative reconstruction from the truncated spin only. (b)–(e): Dual-rotation VOI reconstructions using respectively 4, 9, 37, and 75 additional full-FOV projections. (f): Iterative reconstruction from the full-FOV spin only. Isotropic voxel size: 0.94 mm. Window width is 150 HU.

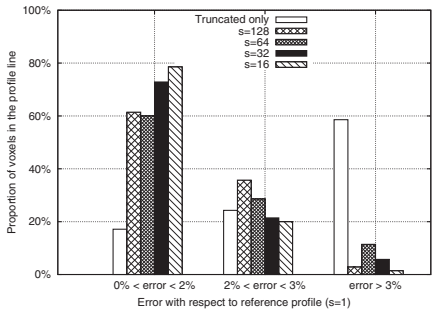

FIG. 10. Deviations from mean profile values along the line profile from Fig. 9(a).

difference between the reprojected image and the truncated data easily implements the extrapolation of the truncated data by the full-FOV acquisition through the image space.[15] Most importantly, we found that an extra apodization is needed to get the desired uniformity in the solution. Note that this step formally makes the criterion nonsymmetrical, but this seems minor as we never experienced any convergence issue.

On a quality assurance phantom and on an anthropomorphic head phantom, images showed superior low-contrast detection and no artifactual trace of being made of two separate spins. High CNR values in 0.94 mm thick slices with dose reduction were obtained at 120 kVp with fixed techniques, a dose ratio of 4, a truncation level of 0.6, and 607 views per spin. These values certainly are beyond the needs of the clinical practice. They primarily illustrate the capabilities of dual-rotation framework and should not be considered optimal.

To provide optimal parameters, we need to take into account all aspects of the system with respect to the targeted clinical task. Let us mention a few. Angular automatic exposure control (AEC) is the norm. Total acquisition time should be as short as possible, so that the truncated spin might be acquired with less views at a faster speed. The scatter contamination depends on the collimated aperture, and the signal read by the detector in the shadow of the collimation provides pure scatter measurement than can be used for scatter correction.[9] Flat-panel detectors limited bit-depth with respect to CT degrades the measured signal and thus the contrast resolution. Electronic noise degrades detection of very low intensities.

The proposed acquisition and reconstruction framework neither requires to know nor estimate the x-ray techniques used by the AEC. It allows for changing the rotation speed between spins, to vary the truncation (potentially dynamically) in order to better handle scatter. The increased number of measurements increases the overall bit-depth, but is more sensitive to electronic noise.

Indeed, for VOI imaging, we did not look at the lowest possible dose per view but rather at vastly undersampling the full-FOV spin. The same algorithm reconstructed the entire field of view with severe distortion outside the VOI but was quite accurate inside when using less than 10 additional views, that is 1/60th of additional views. This is better than what we anticipated when analyzing the literature on VOI imaging with two acquisitions. Our understanding of prior art is that authors searched for a low-dose low-frequency image of the outer field of view to extrapolate the missing low-frequencies. They did not rely on angular undersampling in general, and when they did, they used a sparsity prior to compensate the undersampling.[24,28] On the other hand, authors working on interior tomography, that is without extra measurement, succeeded using "tiny" a priori information.[37–39] Our set-up shows that what is a distorted image of the object outside the field of view still is a faithful enough depiction of the low frequencies whose truncation causes artifacts in the VOI. The polar sampling of the tomographic acquisition does not need many angles to sample those central frequencies; therefore, a least-square criterion does not need extra sparsity a priori to reconstruct the VOI well. The "tiny" a priori can thus be replaced by a "tiny" amount of full-FOV views.

An obvious drawback of C-arm dual-rotation acquisition is that it takes twice as much time and is thus more sensitive to patient motion. Because C-arm detectors have low acquisition frame rates, several rotation speeds are available to yield more or less images for a given acquisition frame rate. Low-contrast resolution requires the maximum angular sampling, thus the lowest speed, but preliminary results were provided where the truncated acquisition was sampled at less angular positions allowing a faster rotation, a configuration that did not require any change in the proposed reconstruction algorithm.

6. CONCLUSION

Dual-rotation C-arm CBCT is a flexible framework that provides high spatial resolution vascular imaging in the clinical routine and is here used in new ways: First, to implement a virtual bow-tie effect and thus increase low-contrast detection, with the added potential benefit of more accurate scatter correction; second to reduce truncation artifacts in the case of VOI imaging. A dedicated least-square iterative algorithm is described that handles all these configurations. High CNR values were obtained on 1% inserts of the Catphan® 515 module in 0.94 mm thick slices. Image quality for VOI imaging was preserved from truncation artifacts even with less than 10 nontruncated views, without using the sparsity a priori common to such context. Results on simulations and acquisitions suggest that this technique has the potential to overcome key performance limitations of C-arm CBCT for brain soft tissue imaging and thus extend the applicability of C-arm CBCT in the field of interventional neuroradiology.

ACKNOWLEDGMENTS

This work was supported by the CIFRE grant No. 873/2014 from the French Association Nationale de la Recherche et de la Technologie (ANRT).

CONFLICTS OF INTEREST

The first three authors are full-time employees of GE Healthcare, Buc, France. Authors have no other conflicts of interest to disclose. The concepts and information presented in this article are based on research and are not commercially available.

[a)]Author to whom correspondence should be addressed. Electronic mail: aymeric.reshef@ge.com.

REFERENCES

1. Anxionnat R, Bracard S, Macho J, et al. 3D angiography. *Neuroradiol*. 1998;25:251.
2. Wunderlich A, Noo F. Achieving uniform noise in direct fan-beam CT reconstruction through bowtie filter design. In: Yu B, ed. *2007 IEEE Nuclear Science Symposium Conference Record*, Vol. 6. Honolulu, HI: IEEE; 2007:4379–4382.
3. Söderman M, Babic D, Holmin S, Andersson T. Brain imaging with a flat detector C-arm. *Neuroradiol*. 2008;50:863.
4. Yu L, Vrieze TJ, Bruesewitz MR, et al. Dose and image quality evaluation of a dedicated cone-beam ct system for high-contrast neurologic applications. *Am J Roentgenol*. 2010;194:W193.
5. Lück F, Kolditz D, Hupfer M, Kalender WA. Effect of shaped filter design on dose and image quality in breast CT. *Phys Med Biol*. 2013;58:4205.
6. Sukovic P, Clinthorne NH. A method for extending the dynamic range of at panel imagers for use in cone beam computed tomography. In: Anthony Seibert J, ed. *Nuclear Science Symposium Conference Record, 2001 IEEE*, Vol. 3. San Diego, CA: IEEE; 2001:1647–1651.
7. Xu J, Sisniega A, Zbijewski W, et al. Evaluation of detector readout gain mode and bowtie filters for cone-beam ct imaging of the head. *Phys Med Biol*. 2016;61:5973.
8. Zellerhoff M, Scholz B, Ruehrnschopf E-P, Brunner T. Low contrast 3D reconstruction from C-arm data. In: Flynn MJ, ed. *Medical Imaging*, San Diego, CA: International Society for Optics and Photonics; 2005:646–655.
9. Siewerdsen J, Daly M, Bakhtiar B, et al. A simple, direct method for x-ray scatter estimation and correction in digital radiography and cone-beam CT. *Med Phys*. 2006;33:187.
10. Yoo S, Yin F-F. *Dosimetric Feasibility of Cone-beam CT-based Treatment Planning Compared to CT-based Treatment Planning*. International Journal of Radiation Oncology, 2006;66:1553.
11. Mail N, Moseley D, Siewerdsen J, Jaffray D. The influence of bowtie filtration on cone-beam CT image quality. *Med Phys*. 2009;36:22.
12. Chityala RN, Hoffmann KR, Bednarek DR, Rudin S. Region of interest (ROI) computed tomography. In: Yaffe MJ, Flynn MJ, eds. *Medical Imaging 2004*, San Diego, CA: International Society for Optics and Photonics; 2004:534–541.
13. Moore CJ, Marchant TE, Amer AM. Cone beam CT with zonal filters for simultaneous dose reduction, improved target contrast and automated set-up in radiotherapy. *Phys Med Biol*. 2006;51:2191.
14. Chen L, Shaw CC, Altunbas MC, et al. Feasibility of volume-of-interest (VOI) scanning technique in cone beam breast CT A preliminary study. *Med Phys*. 2008;35:3482.
15. Cho S, Pearson E, Pelizzari CA, Pan X. Region-of-interest image reconstruction with intensity weighting in circular cone-beam CT for image-guided radiation therapy. *Med Phys*. 2009;36:1184.
16. Schafer S, Noël PB, Walczak AM, Hoffmann KR. Filtered region of interest cone-beam rotational angiography. *Med Phys*. 2010;37:694.
17. Leary D, Robar JL. CBCT with specification of imaging dose and CNR by anatomical volume of interest. *Med Phys*. 2014;41:011909.
18. Parsons D, Robar JL. An investigation of kV CBCT image quality and dose reduction for volume-of-interest imaging using dynamic collimation. *Med Phys*. 2015;42:5258.
19. Parsons D, Robar JL. Volume of interest CBCT and tube current modulation for image guidance using dynamic kV collimation. *Med Phys*. 2016;43:1808.
20. Guan H, Yin F-F, Zhu Y, Kim JH. Adaptive portal CT reconstruction: a simulation study. *Med Phys*. 2000;27:2209.
21. Létourneau D, Wong JW, Oldham M, et al. Cone-beam-CT guided radiation therapy: technical implementation. *Radiother Oncol*. 2005;75:279.
22. Ziegler A, Nielsen T, Grass M. Iterative reconstruction of a region of interest for transmission tomography. *Med Phys*. 2008;35:1317.
23. Kolditz D, Kyriakou Y, Kalender WA. Volume-of-interest (VOI) imaging in C-arm at-detector CT for high image quality at reduced dose. *Med Phys*. 2010;37:2719.
24. Kolditz D, Kyriakou Y, Kalender WA. Low dose, low noise, and high resolution volume of interest (VOI) imaging in C-arm at-detector CT. In: Samei E, Pelc NJ, eds. *SPIE Medical Imaging*, San Diego, CA: International Society for Optics and Photonics; 2010:762226–762226.
25. Kolditz D, Struffert T, Kyriakou Y, Bozzato A, Dörer A, Kalender W. Volume- of-interest imaging of the inner ear in a human temporal bone specimen using a robot-driven C-arm at panel detector CT system. *Am J Neuroradiol*. 2012;33:E124.
26. Ritschl L, Knaup M, Kachelrieß M. Extending the dynamic range of at detectors in CBCT using a compressed-sensing-based mulit-exposure technique. *Proc Fully 3D*. 2013;3:26.
27. Lu W, Yan H, Gu X, et al. Reconstructing cone-beam CT with spatially varying qualities for adaptive radiotherapy: a proof-of-principle study. *Phys Med Biol*. 2014;59:6251.
28. Kästner T, Hornegger J, Maier A, Xia Y, Bauer S. Truncation robust C-arm CT reconstruction for dynamic collimation acquisition schemes. In: Handels H, Deserno T, Meinzer HP, Tolxdorff T, eds. *Bildverarbeitung für die Medizin 2015*, Lübeck, Germany: Springer; 2015:516–521.
29. Maaß C, Knaup M, Kachelrieß M. New approaches to region of interest computed tomography. *Med Phys*. 2011;38:2868.
30. Feldkamp L, Davis L, Kress J. Practical cone-beam algorithm. *JOSA A* 1984;1:612.
31. Parker DL. Optimal short scan convolution reconstruction for fan beam CT. *Med Phys*. 1982;9:254.
32. Langet H, Riddell C, Reshef A, et al. Compressed-sensing-based content-driven hierarchical reconstruction: theory and application to C-arm cone-beam tomography. *Med Phys*. 2015;42:5222.
33. Riddell C, Benali H, Buvat I. Diffusion regularization for iterative reconstruction in emission tomography. *IEEE Trans Nucl Sci*. 2004;51:712.
34. Zeng GL. Revisit of the ramp filter. *IEEE Trans Nucl Sci*. 2015;62:131.
35. Goodenough D. *Catphan 500 and 600 Manual*. Greenwich, NY: The Phantom Laboratory 2012.
36. Lauritsch G, Boese J, Wigstrom L, Kemeth H, Fahrig R. Towards cardiac C-arm computed tomography. *IEEE Trans Med Imaging*. 2006;25:922.
37. Kudo H, Courdurier M, Noo F, Defrise M. Tiny a priori knowledge solves the interior problem in computed tomography. *Phys Med Biol*. 2008;53:2207.
38. Kudo H, Suzuki T, Rashed EA. Image reconstruction for sparse-view ct and interior ctintroduction to compressed sensing and differentiated backprojection. *Quant Imaging Med Surg*. 2013;3:147.
39. Wang G, Yu H. The meaning of interior tomography. *Phys Med Biol*. 2013;58:R161.